

Advancement of the Segment Support System for the Thirty Meter Telescope Primary Mirror[†]

Eric C. Williams*^a, Curtis Baffes^b, Terry Mast^c, Jerry Nelson^c, Benjamin Platt^b, RJ Ponchione^d, Eric Ponslet^e, Shahriar Setoodeh^e, Mark Sirota^a, Vince Stephens^d, Larry Stepp^a, Alan Tubb^d.

^aTMT Observatory Corporation, 2632 East Washington Blvd, Pasadena, CA, USA 91107;

^bJet Propulsion Laboratory, California Institute of Technology, 4800 Oak Grove Dr., Pasadena, CA, USA 91109;

^cCenter for Adaptive Optics, University of California, Santa Cruz, USA 95064;

^dHYTEC, Inc., 110 Eastgate Drive, Los Alamos, NM, USA 87544

^eFormerly HYTEC, Inc.

ABSTRACT

This paper presents refinements to the design of the TMT primary mirror segment passive-support system that are effective in reducing gravity print-through and thermal distortion effects. First, a novel analytical method is presented for tuning the axial and lateral support systems in a manner that results in improved optical performance when subject to varying gravity fields. The method utilizes counterweights attached to the whiffletrees to cancel astigmatic and comatic errors normally resulting when the lateral support system resists transverse loads induced by gravity. Secondly, several central diaphragm designs are presented and analyzed to assess lateral-gravity and thermal distortion performance: 1) a simple flat diaphragm, 2) a stress-relieving diaphragm having a slotted outer rim and a circumferential convolution near the outside diameter, and 3) a flat diaphragm having a slotted outer rim. The latter design is chosen based on results from analytical studies which show it to have better overall optical performance in the presence of gravity and thermal environments.

Keywords: telescope, mirror, segment, deformation, distortion, support, whiffletree, diaphragm, counterweight, thermal

1. INTRODUCTION

The Thirty Mirror Telescope (TMT^[1]) Project, a partnership between ACURA, Caltech, and the University of California, is currently developing a 30-meter diameter segmented optical telescope. The initial development of the TMT Segment Support Assembly (SSA) was presented in a previous paper^[2], which detailed the axial support system optimization, lateral support system trade studies, warping harness performance, and hardware design concepts. Subsequently, the segment dimensions have been changed from 1.2m across the vertices by 40mm thick to 1.44m by 45mm thick. This paper focuses on the opto-mechanical performance of the larger segment size subjected to gravity and thermal environments. Specifically, improvements to the support system design that minimize lateral gravity distortion, while mitigating thermal distortion are presented.

The segmented TMT Primary Mirror, Figure 1, will be composed of 492 independent, low expansion glass segments, nominally separated by 2.5 mm gaps. The array has six-fold symmetry, and thus six identical sectors of 82 unique segment types. Each segment is hexagonal, cut from an aspherical meniscus, with a 0.72 meter nominal side length, and a thickness of 45 mm. Because it is not possible to divide a curved mirror surface into identical, regular hexagons, the precise shapes of the segments have been optimized using a radial scaling relation. This approach is described in a companion paper in this conference³.

For each segment, a local SSA coordinate system is defined as shown in Figure 1. The design of the SSA is performed in this coordinate system. Throughout the remainder of this paper, and unless otherwise indicated, all reference is to this coordinate system.

*ewilliams@tmt.org; phone 1-626-395-1638; fax 1-626-395-8909

† SPIE 7018-37, TMT.OPT.JOU.08.004.REL01

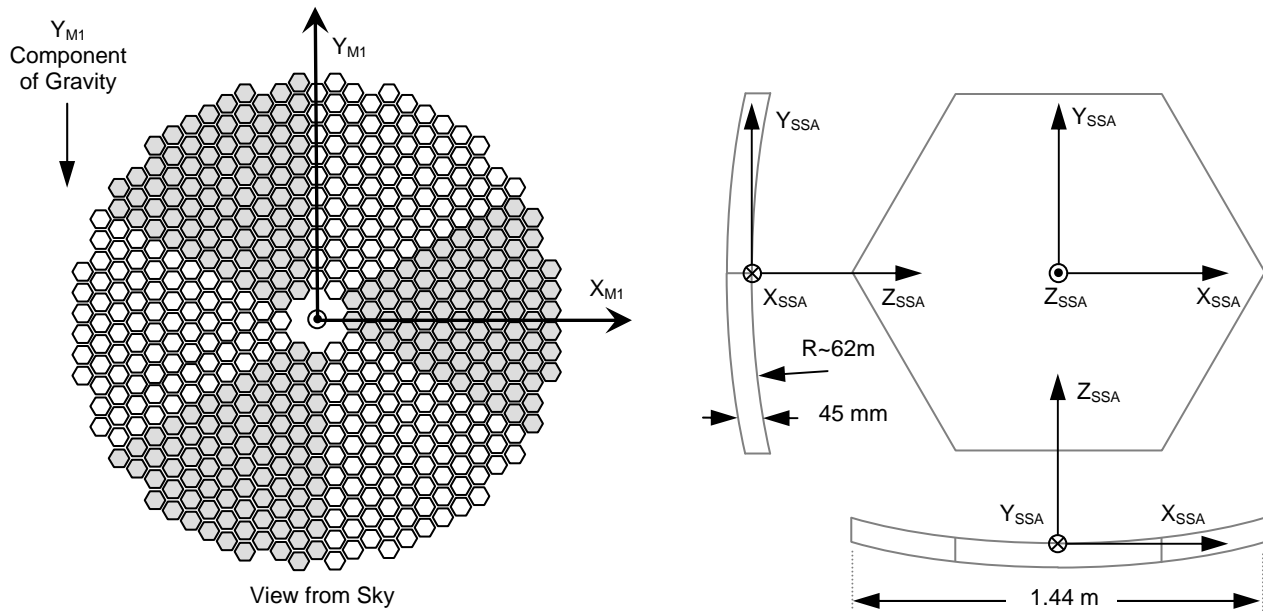


Figure 1 TMT Primary mirror segmentation, nominal segment geometry, and definition of global (M1) and local (SSA) reference frames.

2. SUPPORT SYSTEM DESCRIPTION

To achieve the required surface accuracy and stability (less than 20 nm RMS surface figure error from support-induced deformations) each segment will be supported by a multi-point, passive, near-kinematic system, which is actively controlled in piston, tip and tilt by a set of three linear actuators, and figure-controlled by an automated warping harness. The segment and support system design are shown schematically in Figure 2.

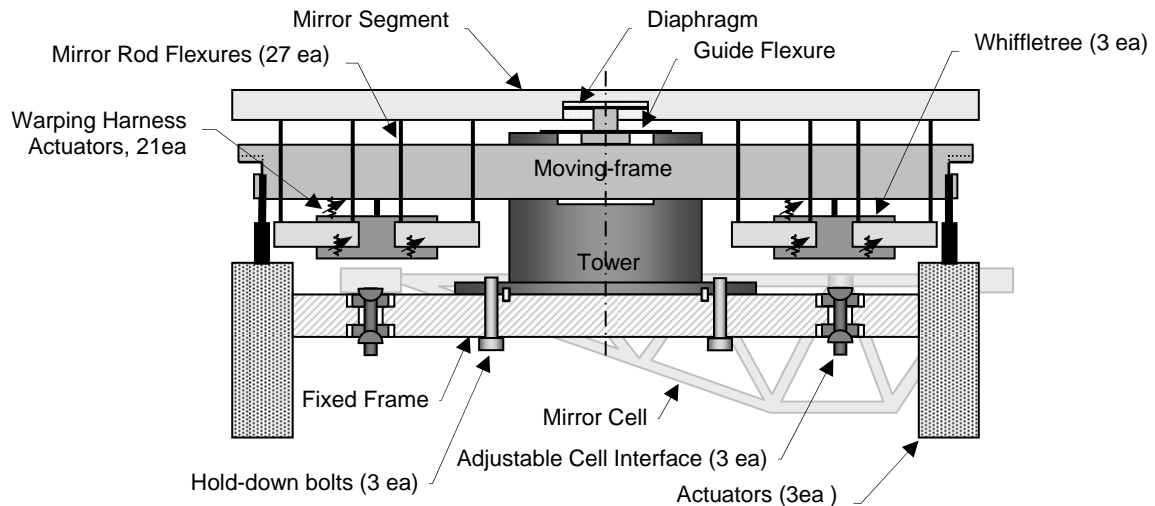


Figure 2 Schematic of the TMT primary mirror segment and support system.

The TMT segment support design, shown in Figure 3 and Figure 4, is largely based on concepts developed for other segmented mirrors. It is an evolution of the Keck^[4,5] designs, with some features adopted from the Southern African Large Telescope (SALT^[6,7,8,9]). Even though large segmented telescopes are only about 20 years old, the technological approaches to segment support are relatively well established. Almost every segmented telescope project, since Keck, has used mechanical whiffletrees for axial support, and a central diaphragm lateral support.

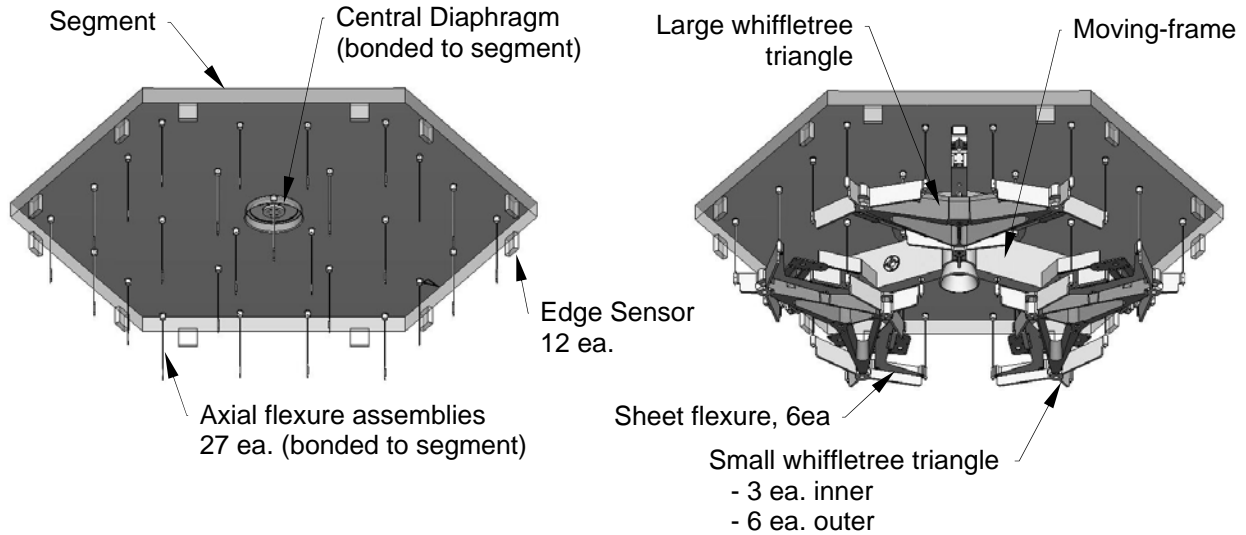


Figure 3 Hexagonal mirror segment shown with axial support flexures, central diaphragm, edge sensors (left), and whiffletrees, sheet-flexures and moving-frame (right).

In contrast with earlier segmented telescopes of the 10-meter class, such as Keck, the much larger size of the TMT primary mirror will result in increased gravity-induced deflections of the primary mirror cell, requiring larger actuator strokes to maintain segment phasing. The TMT primary mirror segments will also be thinner than previous large telescopes, making control of gravity-induced deflections a more difficult problem. These characteristics favored a moving-frame support concept^[9] which was first introduced by the designers of the Southern African Large Telescope (SALT). In this approach, an intermediate, stiff *moving-frame* is used to isolate the segment from the relatively large flexure reactions which result from the large actuator motions. The moving-frame, supported in-plane by a guide-flexure, absorbs these loads. The whiffletrees are supported laterally by the moving-frame, through a set of *sheet-flexures*. The sheet-flexures provide a stiff in-plane load path between the whiffletree triangles and the moving-frame, while preserving whiffletree kinematics by way of their out-of-plane flexibility.

The whiffletrees, sheet-flexures, and moving-frame are made from aluminum. The 27 rod flexures supporting the mirror and the pivots within the whiffletrees are stainless steel. The central diaphragm and the pucks that connect the rod-flexures to the glass segment are made from Invar-36. All metal-to-glass connections are made using epoxy adhesive.

Each of the 82 unique segment types has slightly different dimensions. These differences are accommodated in the support system design by small differences in the positions of the whiffletree pivot connections. The results presented in this paper are for the nominal average segment shape, but they are representative of the performance of each type.

An automated warping harness with 21 actuators per segment will provide the ability to remotely alter the surface figure of each segment to correct for effects such as coating stresses, figuring errors, lateral position errors, seasonal temperature fluctuations, and through-the-thickness variations of the coefficient of thermal expansion of the glass.

Finally, given the unprecedented number of segments in TMT (492 + 82 spares), cost control is a major consideration in the design process. The target cost of TMT is less than half of the scaled-up Keck cost. This places very stringent requirements on fabrication costs in every subsystem. In the case of the SSA, the relatively large number of replications of an identical assembly presents an opportunity to consider mass production approaches, which will help control costs.

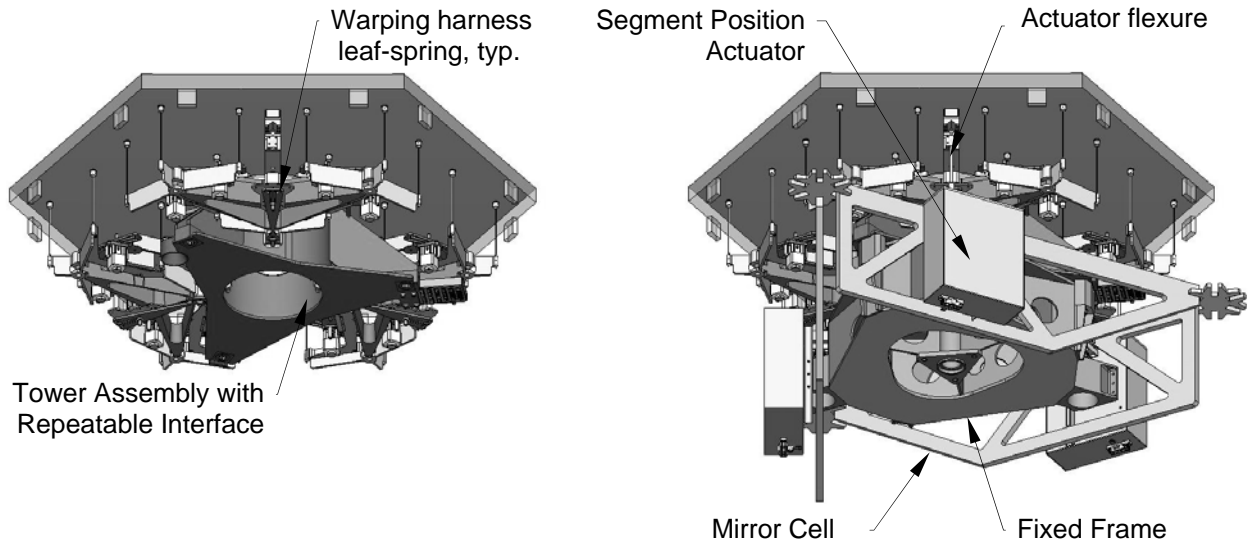


Figure 4 The Polished Mirror Assembly (left) mounts to fixed frame and actuators which are supported by the mirror cell (right). The Polished Mirror Assembly is removed from the telescope for re-coating of the optical surface.

3. PERFORMANCE PREDICTIONS

The performance of the telescope is strongly influenced by the performance of the SSA subjected to varying gravity and temperature fields. These effects are considered in the design and analysis of the SSA, and in some cases tradeoffs of one performance characteristic against another are required. For example, it is possible to minimize the thermal distortion response of the segment at the expense of the lateral gravity performance. The character of the surface errors is also an important factor in assessing the relative merit of a particular design. For example, low spatial frequency errors are more easily tolerated because they impact the seeing-limited performance to a lesser degree than high frequency errors of the same RMS magnitude. Similarly, the telescope Adaptive Optics system has the ability to compensate for low spatial frequency errors, but not for higher frequency errors. Thermal distortion errors typically contain a significant component of focus which is better tolerated than higher frequency errors from axial or lateral gravity print-through.

TMT intends to final-figure and acceptance-test segments after they are attached to their support systems, with the segments zenith-pointing, and at the mean observing temperature. By figuring in this manner, the distortion due to axial gravity and assembly pre-stresses can be removed, along with a significant portion of the thermal distortion. Therefore, all performance predictions are relative to the final-figured condition. This also implies that the axial surface error springs back as the segment is inclined from the local zenith ($\zeta_{SSA}=0$) as $[1-\cos(\zeta_{SSA})]$, with the lateral print-through increasing from zero at the zenith in proportion to $[\sin(\zeta_{SSA})]$. Thermal distortion is proportional to the temperature difference between the acceptance test temperature and the segment temperature during observing.

3.1 System-level Finite Element Simulations

A system-level finite element model, Figure 5, was developed to provide an integrated approach to assessing the optical performance, strength, and stability of the SSA. The system model, developed using FEMAP^[10] and solved using NX-NASTRAN^[11], captures the following important effects which improve the quality of predictions:

- Combined interaction of the axial and lateral support systems
- Compliance of the many structural components, important for optical and dynamic performance predictions

- Aggregate thermal expansion (axial and radial) of the support systems
- Warping harness stiffening of the whiffletree mechanism, making the system less kinematic
- Mirror cell top chord members and the SSA fixed frame

The system model reflects the preliminary design, incorporating an optimized 27-point axial support topology and central diaphragm lateral support. The system model is a high fidelity representation of the preliminary design, constructed to ensure that all important effects and interactions are represented.

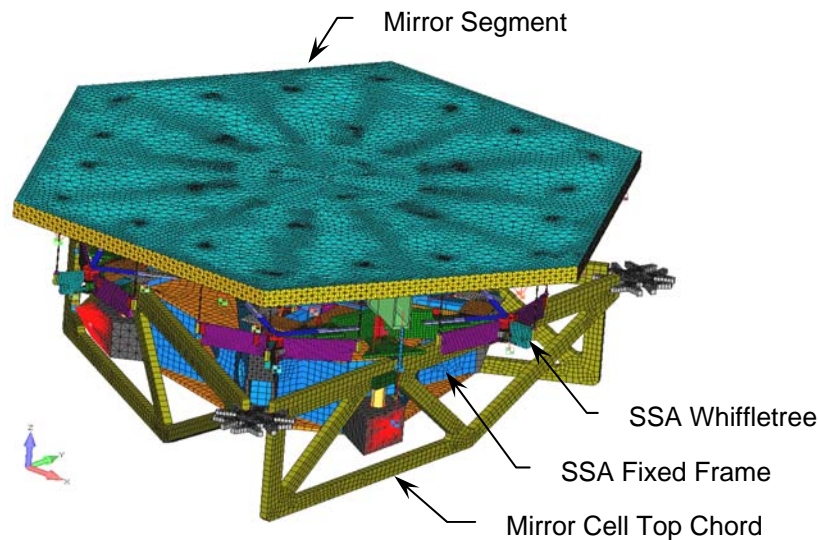


Figure 5 System-level finite element model of segment, SSA, actuators, and mirror cell.

3.2 Axial support performance

A comprehensive investigation and systematic numerical optimization^[2] lead to the selection of the 27-point axial support whiffletree for the previous 1.2m segment. The motivations for the 27-point topology, shown in Figure 6, were twofold: 1) the axial support print-through surface error could be economically minimized, and 2) the warping harness performance, based on the 27 point whiffletree, satisfied performance requirements. Whiffletrees having fewer support points, or other arrangements of the 27-points, did not perform as well. Support systems with more than 27 points require an additional whiffletree layer, which can improve performance but at significant cost in terms of part count, complexity, and production expense.

Since the publication of the previous studies^[2], the segment size was increased from 1.2m to 1.44m to reduce manufacturing cost and part count, improve telescope reliability, and lower the long-term operating cost of the observatory. Simultaneously, with the size increase, a decision was made to increase the thickness of the segments to 45 mm. It was recognized that this combination of size and thickness would result in slightly increased surface figure error compared to the previous design. This is an expected result, given that for a thin circular plate subject to transverse bending due to self weight, the surface deformation scales as $[a^4/t^3]$, where a is the radius and t is the thickness. Therefore, the mirror would need to be ~51mm thick to maintain the same axial gravity performance as the 1.2m by 40mm thick design. The motivations for limiting the thickness increase include the desire to keep the mass and thermal inertia of the primary mirror as low as practical, and to also control the cost of the mirror blanks.

Since the whiffletree optimization was performed on an idealized finite element model, it was necessary to re-tune the whiffletree to account for numerous physical effects that cause the real system to behave slightly differently than the idealized model. These effects include: mass and stiffness perturbations introduced by the central diaphragm support

hole, edge sensor masses, small axial loads transmitted through the lateral support central diaphragm, and slight non-kinematic behavior within the whiffletrees. The tuning is accomplished by optimizing the in-plane position of the twelve whiffletree pivots to minimize axial-gravity (g_z) induced surface error. (The set of twelve pivots consists of nine pivots connecting the small whiffletree triangles to the large whiffletree triangles, and three pivots that connect the large whiffletree triangles to the moving-frame.) The adjustments are calculated using a perturbation technique, and implemented physically by shifting the in-plane locations of the whiffletree pivots. After tuning the axial support system in this manner, the surface error predicted by the system-level model is 10.4nm RMS, as shown in Figure 6. As described previously, this error is figured-out with the segment zenith-pointing, and springs-back as the segment is tilted to the horizon.

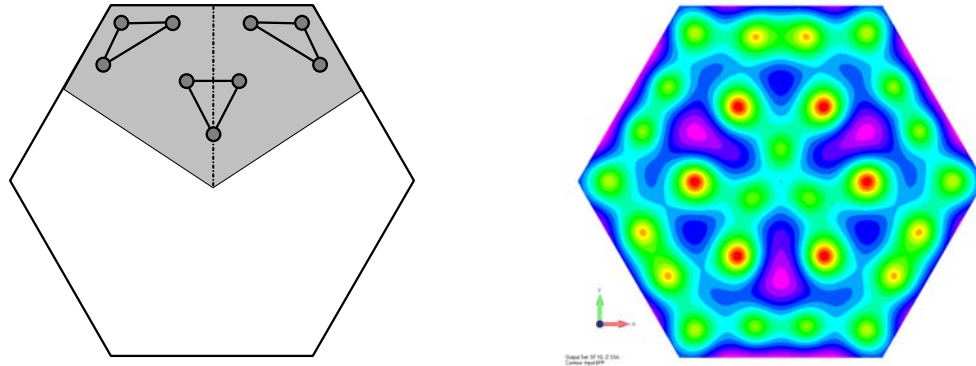


Figure 6 TMT whiffletree support-point topology (left) and predicted surface error resulting from axial gravity, $1g_z$ (right). Predicted surface error is 10.4nm RMS and 60nm peak-valley. Purple = -11nm, Red = +49nm. (Piston/Tip/Tilt subtracted)

3.3 Lateral support performance

Given a thin meniscus mirror laterally supported at one or more discrete points and subject to lateral gravity, the curvature of the neutral axis results in distributed bending moments acting across the span. These distributed internal moments result in bending of the mirror and distortion of the optical surface. Additional effects associated with local attachments can result in additional distortions of the optic.

A central lateral support can be installed at a given depth below the optical surface by machining a pocket (blind hole) into the back of the mirror. If the center support is aligned (in the thickness direction, Z) with the center of mass of the mirror, there is zero net overturning moment on the mirror. If the center support is located to either side of the center of mass, there will be a net overturning moment that must be reacted. For the TMT design, a central diaphragm is bonded to the bottom of the pocket, forming the center support, and the whiffletrees react any overturning.

The conventional approach for designing a support system having independent axial and lateral supports is to support and balance the whiffletrees such that they exert no overturning moments onto the optic as the zenith angle is changed. All lateral loads are reacted by the center support while the whiffletrees stabilize the optic in tip/tilt, and react any induced or externally applied overturning moments. Using this approach, the optimum diaphragm location is determined that minimizes the surface RMS. This optimum location is offset from the neutral axis, slightly closer to the concave optical surface by fractions of a millimeter, giving 20.8nm surface RMS due to lateral gravity ($1g_x$ and $1g_y$). The Zernike decomposition of this surface shape, calculated using SigFit^[12], is shown in Table 1a. The 20.8 nm RMS result is not adequate for TMT, so further work was performed to find a solution with better performance.

3.4 Interaction of axial and lateral supports

In an effort to reduce this print-through error, we consider imposing additional moments into the system via whiffletree imbalance. Notionally, a new optimum can be found that includes some amount of whiffletree-based loading that will

beneficially counteract some of the bending deformation resulting from the meniscus shape. To minimize the complexity of the scheme, only moments introduced at the large whiffletree triangles are considered. (Note: the large triangles are the load spreaders that connect the moving-frame to the three small triangles in each whiffletree, as shown in Figure 3). Whiffletree moments introduced at the large triangles produce global, low order deformations. When the Zernike content of the whiffletree moment case is examined, Table 1b, a large amount of astigmatism and a lesser amount of coma, in the ratio of approximately 6:1, are seen.

Exploring the character of the 20.8nm surface figure, significant amounts of coma and astigmatism are found but in a different ratio, as shown in Table 1a. As the diaphragm axial location and pocket depth are varied, the amount of astigmatism and coma vary linearly. At one diaphragm location, the ratio of astigmatism to coma is approximately -6:1, which is the inverse to the whiffletree moment effect.

Aberration	(a) 1gx - Classical Optimization (without whiffletree moments)		(b) Whiffletree Moments $M_y = 1 \text{ N-m per WT}$		(c) 1gx - Re-optimized (with whiffletree moments)		(d) Magnitude Reduction $ \text{Mag}_a - \text{Mag}_c $
	Mag. nm	Phi (Deg)	Mag. nm	Phi (Deg)	Mag. nm	Phi (Deg)	$\Delta\text{Mag.}$ nm
Input(wrt zero)							
Bias	-0.05	0.0	0.00	0.0	0.01	0.0	0
Tilt	19.46	-0.1	6.15	180.0	6.80	-0.3	13
Focus	-0.28	0.0	0.00	0.0	0.02	0.0	0
Pri Astigmatism	-14.97	-45.2	154.10	-45.0	2.27	-48.0	13
Pri Coma	-55.48	179.9	24.94	180.0	6.08	-1.2	49
Pri Trefoil	0.09	-16.0	0.00	50.8	0.15	1.1	0
Pri Spherical	0.01	0.0	0.00	0.0	0.01	0.0	0
Sec Astigmatism	1.52	-44.7	17.59	45.0	1.75	44.6	0
Pri Tetrafoil	0.12	18.1	8.63	22.5	0.66	-23.0	-1
Sec Coma	7.66	179.9	10.60	0.0	12.15	0.2	-4
Sec Trefoil	0.03	57.7	0.00	49.2	0.05	-58.7	0
Pri Pentafoil	15.72	-36.0	2.77	-36.0	17.71	-36.0	-2
Sec Spherical	-0.07	0.0	0.00	0.0	0.01	0.0	0
Ter Astigmatism	0.14	47.6	1.65	-45.0	0.34	-45.8	0
Sec Tetrafoil	0.03	20.8	0.62	22.5	0.44	22.6	0
Pri Hexafoil	0.08	0.0	0.00	-29.4	0.02	29.5	0
Ter Coma	41.18	-0.1	3.80	180.0	28.54	-0.2	13
Ter Trefoil	0.05	-13.3	0.00	26.9	0.04	-0.9	0
Sec Pentafoil	8.58	-36.0	0.52	-36.0	7.30	-36.0	1
Ter Spherical	-0.05	0.0	0.00	0.0	0.02	0.0	0
Qua Astigmatism	0.00	13.4	2.98	45.0	0.61	45.1	-1
Ter Tetrafoil	0.08	21.3	1.77	22.5	0.39	22.7	0
Sec Hexafoil	0.04	1.1	0.00	-21.5	0.01	27.9	0

Table 1 Zernike fit of optical surface shape for:
a) $1g_x$ lateral load case for classically optimized design, before correcting with whiffletree moments (diaphragm located 0.045mm above mirror neutral axis)
b) whiffletree moment case ($M_y = 1.0 \text{ N-m}$ at three whiffletree locations)
c) $1g_x$ lateral load case for re-optimized design using whiffletree moments
d) Difference between classical results (a) and re-optimized design (c), $\Delta\text{Mag} = |\text{Mag}_a| - |\text{Mag}_c|$.

Figure 7 shows the influence of diaphragm position on astigmatism, coma, the ratio of astigmatism to coma, uncorrected surface RMS (without the whiffletree moments included), corrected surface RMS (including the whiffletree moments) and finally, thermal distortion surface RMS. The curve representing corrected RMS shows a new minimum (~12nm RMS) which is significantly lower than the previous minimum (~20.8nm RMS). The new minimum corresponds to a diaphragm position that is approximately 1.755mm below the mid-plane of the segment. It is noted that the true minimum is not precisely where the astigmatism to coma ratio is 6:1. Since the gravity-induced surface error and the correcting moments also affect the high frequency terms, beyond astigmatism and coma, it is not surprising that

the optimum solution is not exactly where the ratio is 6:1, but nearby. The Zernike decomposition of this new minimum, (re-optimized) is shown in Table 1c.

The absolute difference in the Zernike coefficients between the classical result (1a) and the re-optimized design (1c) is shown in Table 1d. Note that this new solution has significantly less Primary Astigmatism, Coma, and Tertiary Coma. For the terms shown, only a few terms show small increases in amplitude. These results demonstrate that the approach significantly reduces global bending at no other apparent optical consequence.

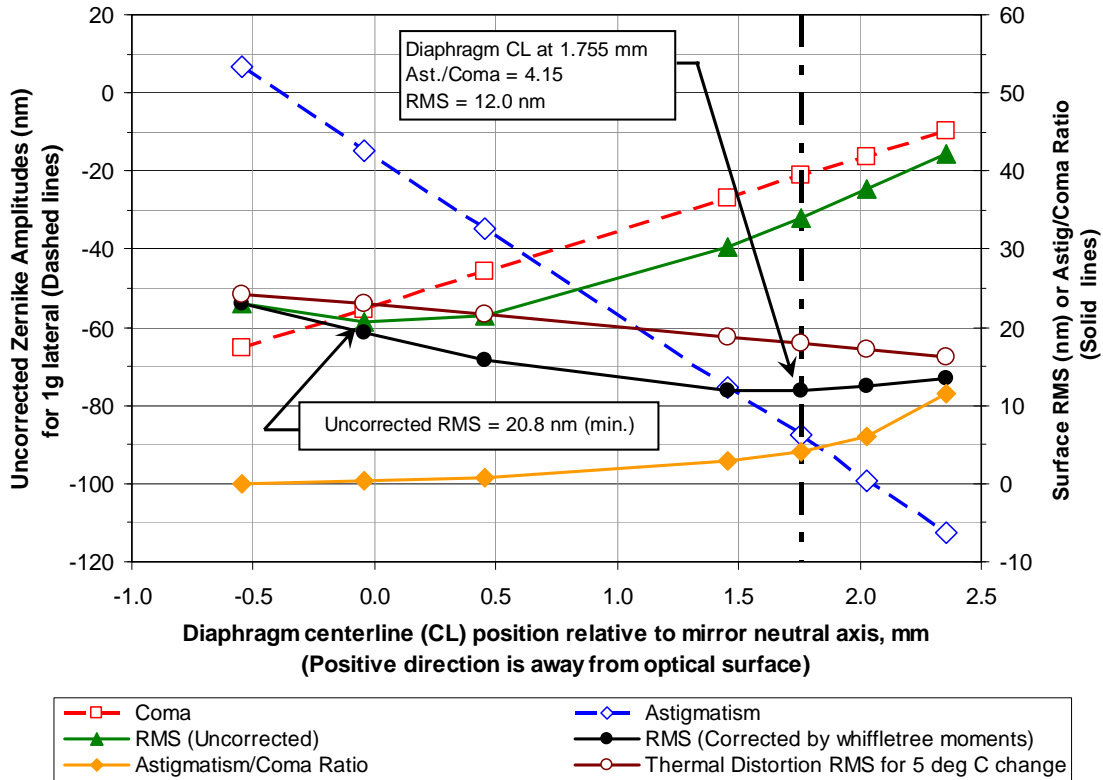


Figure 7 Results for $1g_x$ loading: astigmatism, coma, astigmatism to coma ratio (all before correction); surface RMS corrected and uncorrected. Thermal distortion for 5°C temperature change. All predictions as a function of diaphragm position. (Piston/Tip/Tilt subtracted)

Also shown in Figure 7 is the predicted thermal distortion resulting from an isothermal temperature change applied to the segment and SSA. The thermal distortion arises because of the coefficient of thermal expansion (CTE) mismatch between the SSA and the glass. The analysis assumes a 5°C temperature change, which is representative of the statistical variations about the median observing temperature at the site. It is noted that the thermal distortion decreases as the diaphragm is shifted slightly away from the optical surface, over this range of diaphragm positions. This effect is an additional benefit of utilizing the new minimum.

Another design option that was considered is to position the diaphragm such that the thermal distortion is minimized. Such a solution was explored, and it was found that the thermal distortion could be driven close to zero, but at the expense of large lateral gravity distortions. Since the optical performance of the telescope is more sensitive to high frequency errors, such as lateral distortion, it is clear that this approach does not provide a preferred solution for TMT.

3.5 Implementation and analytical verification

The new preferred design has the revised diaphragm location, and a set of counterweights added to the large whiffletree triangles to produce the correcting moments associated with the new diaphragm location. The magnitude of the whiffletree moments required to minimize the surface RMS is approximately 0.7 Nm, which corresponds approximately to a 1 kg mass offset from the sheet flexure line-of-action by 60mm for each of the three large triangles. In practice, four small counterweights will be added to each large whiffletree triangle to produce the desired whiffletree moment due to lateral gravity (g_x & g_y), while preserving the tip/tilt balance of the triangle when subject to axial gravity (g_z). By preserving the tip/tilt balance, the axial gravity performance is essentially unchanged at 10.4nm RMS.

The counterweights are included in the system-level model and the solution is verified by solving the three unit gravity cases as shown in Figure 8. These results confirm the axial gravity response is unchanged, while the lateral gravity cases show significant improvement, with the surface RMS reduced to ~12.0 nm.

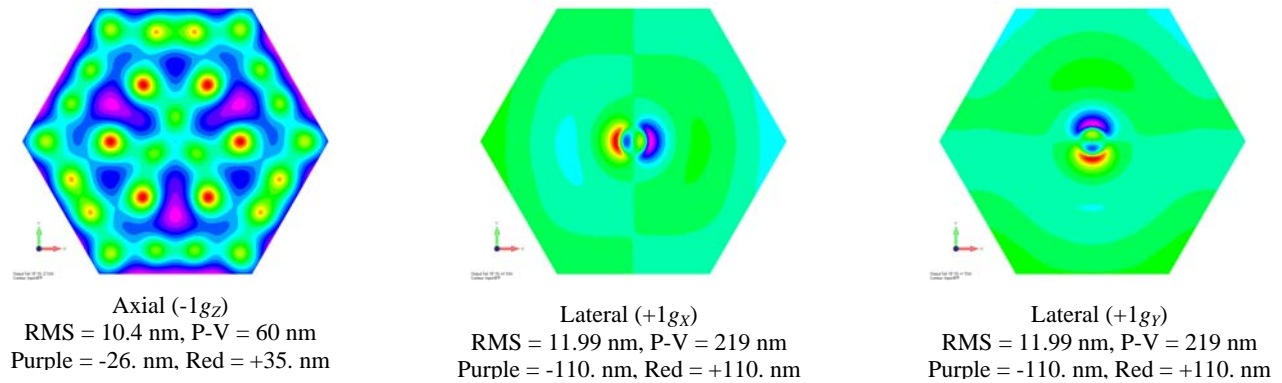


Figure 8 Surface distortion plots for three unit gravity load cases from the system-level model modified to have the new optimum diaphragm position and large whiffletree triangle counterweights. (Piston/Tip/tilt subtracted)

4. CENTRAL DIAPHRAGM TRADE STUDIES

The lateral support central diaphragm provides the primary lateral load path, supporting the segment as the telescope tilts toward the horizon. For TMT, the Invar diaphragm is bonded directly to the glass segment at the bottom of the pocket, as shown in Figure 3 and Figure 9. This approach was chosen because it is simple, compact, and low cost, not requiring additional de-coupling flexures between the diaphragm and the glass. Since the segments are fabricated from low expansion glass, having CTEs near zero, the diaphragms are made from Invar, which also has a low CTE. However, compared to the low expansion glass, Invar's CTE (approximately 1.3 ppm/°C) still causes stress at the glass interface, as well as distortion of the optical surface as the temperature of the assembly varies during operation, with respect to the reference conditions. Several diaphragm concepts have been studied to find a design that moderates the CTE mismatch effects, while providing a stiff, strong load path and acceptable lateral gravity optical performance.

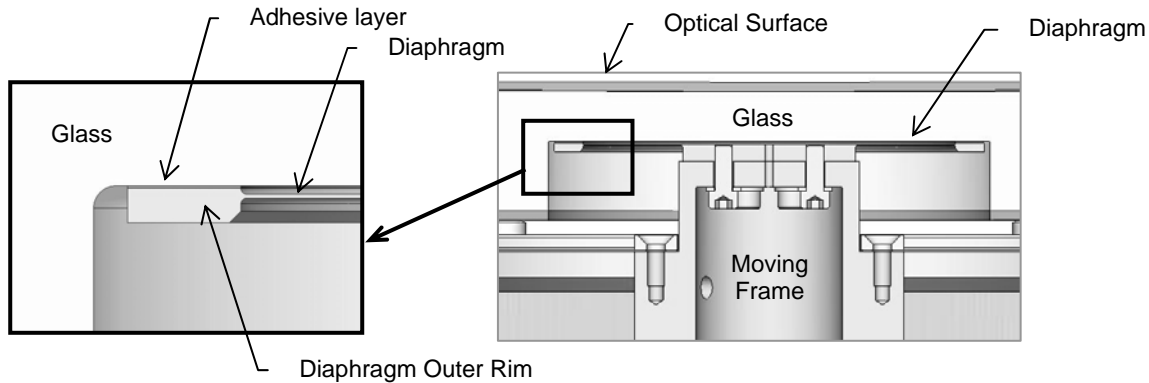


Figure 9 Cross-section view showing diaphragm outer rim bonded to the glass segment at the bottom of a machined pocket, and bolted connection between diaphragm center hub and moving-frame.

4.1 Diaphragm Concepts

All of the diaphragm concepts studied share three basic features. Each has a center hub which provides a stiff, strong connection to the moving-frame via a bolted connection. Each diaphragm also has a thin flexible region that is outboard of the hub. This thin region is sized to provide the greatest amount of axial compliance, while retaining sufficient lateral stiffness, strength, and elastic stability to support the segment during operation and survival events such as handling, transportation, and seismic. The third common feature is a thickened outer rim that is bonded to the glass. The thicker section is included to improve load transfer, minimize bond peel stress, and ease manufacturing and assembly. There is a recessed area between the glass and the thin flexible region to permit the diaphragm to deflect during operation without contacting the glass at the bottom of the pocket.

In this discussion, temperature increases affecting the system will be referenced, recognizing that a temperature decrease causes the opposite response. When subject to a temperature increase, thermal mismatch loads develop between the glass and the diaphragm as the diaphragm tries to expand radially, while the expansion is resisted by the low expansion glass. A design that minimizes the effects of CTE mismatch is sought. In this light, the three diaphragm designs shown in Figure 10 were considered. All three designs are fabricated from a single piece of Invar. Their features and inherent characteristics will be described, and then the analysis results that lead to selecting the preferred design for TMT will be presented.

The first diaphragm concept (Option-1) is a simple, flat diaphragm, having a continuous outer rim. This diaphragm is the simplest and lowest cost design. Analysis shows that it produces the largest CTE mismatch loads, and hence largest stress and optical distortion as the temperature changes. When subject to lateral gravity, this diaphragm transfers loads in an effective manner, helping minimize distortion of the optical surface.

The second diaphragm concept (Option-2) was developed to reduce the CTE mismatch effects by adding two additional features. First, there is an axisymmetric convolution extending around the perimeter near the outside diameter of the flexible region. This flexible convolution allows the thin flat region of the diaphragm to expand radially, without imparting significant radial forces into the glass. Second, the outer rim has a pattern of radial slots that interrupt the hoop continuity of the outer rim, greatly reducing the loads transmitted into the glass. The combination of the convolution and the slots results in a very low stress design in terms of CTE mismatch. Stiffness and strength are only slightly degraded for this design, but the part is more complex and costly to fabricate. Additionally, the slotted rim results in a set of tabs that must be bonded to the glass, rather than the continuous rim of the first concept. Analysis shows this design to be extremely good from a thermal distortion standpoint, compared to the first design, but deficient when subject to lateral gravity.

The third diaphragm concept (Option-3) is a compromise between the first two designs, having a slotted outer rim, but no convolution. Analysis shows this design to have moderately better thermal distortion, compared to the first design, and essentially the same optical performance when subject to lateral gravity.

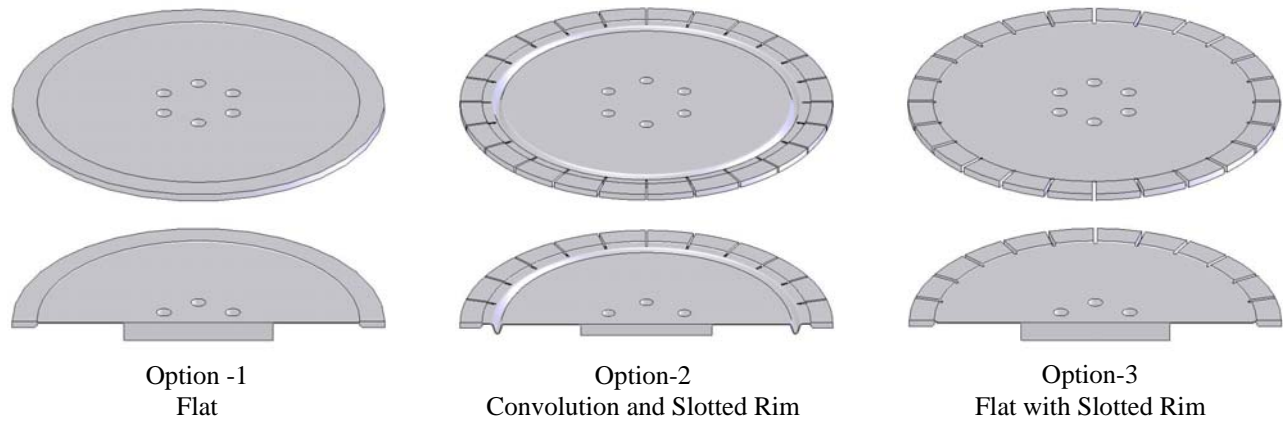


Figure 10 Three lateral support diaphragm Options considered for TMT. Each design is shown from the mirror side (top), and cross-sectioned (bottom).

4.2 Component-level analyses

Before the system-level optical performance of these competing designs can be analyzed and compared, the diaphragms must be sized to transmit the design loads. All three diaphragms are buckling-controlled designs. Elastic stability of the diaphragm is required (shall not buckle) when the system is subjected to a 2g static lateral load, and in the post-buckled range, elastic behavior up to 3g is required. Component-level analysis can be used to provide insight into the performance and characteristics of these designs. In comparing the component-level analysis results, two areas of performance were observed that are different between the designs: thermal-mismatch interface loads, and the load-path for carrying in-plane loads.

4.2.1 Thermally-induced interface loads

Interface loads due to thermal mismatch for Option-1 and Option-2 were calculated from FEA unit-case results by summing the radial component of nodal forces at the adhesive interface to the optic. The Option-2 design (with convolution and slots) produced an integrated radial force that is one tenth that produced by the flat diaphragm, (Option-1). The reduction of thermally induced interface forces results in improved thermal distortion performance for Option-2. The Option-3 design shows interface forces that are less than the Option-1 design, but greater than the Option-2 design.

4.2.2 Lateral gravity load path and interface stress

The convolution feature included in the Option-2 diaphragm has an effect on the in-plane load path and stiffness. As the predicted adhesive stress distributions show in Figure 11, the load transfer patterns are very different for the flat diaphragms as compared to the diaphragm with the convolution and slots.

Both flat diaphragms transfer the applied load to the bond-line along the line-of-action of the applied load (the 12- and 6-o'clock positions in the figures on the left and right). The load is transferred in this manner because the tension/compression fields are the stiffest load path within the diaphragm sheet. The shear load path (at 3- and 9-o'clock) is less stiff and attracts a significantly smaller portion of the load (recall the shear modulus of most metals is typically $\sim 1/3$ of the tensile modulus).

When the convolution is added to the diaphragm (Option-2), the radial load path (tension/compression) is substantially decoupled, making the shear load path dominant. This results in very little load being transferred at the 12- and 6-o'clock positions, with most of the load being transferred at the 3- and 9-o'clock locations.

We will show in Section 4.3.2 that these different load paths result in important optical consequences for the segment when subject to lateral gravity.

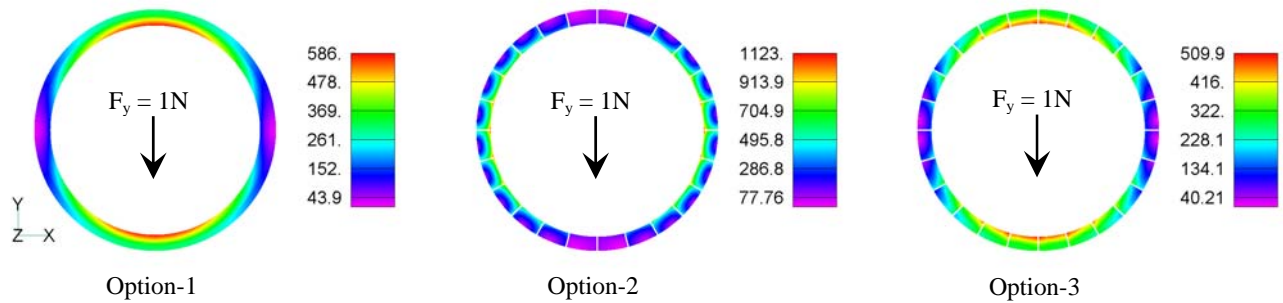


Figure 11 Diaphragm-to-mirror adhesive stress contour plot (Max shear stress, Pa) resulting from 1N unit load. Option-1, flat with continuous rim (left), Option-2, convolution and slots (center), and Option-3, flat with slotted rim (Right)

In addition to the difference in the load transfer mechanism, the convolution also alters the in-plane stiffness of the diaphragm, reducing the stiffness by approximately 50% compared to the flat diaphragms. The stiffness of all three diaphragm types is adequate for TMT.

Comparing the stress magnitudes associated with each design shown in Figure 11, shows that Option-2, with the convolution and slots, produces twice the adhesive stress at the interface to the glass. For Option-2, the slotted rim bond tabs near the 3- and 6-o'clock locations are subject to shear loads and in-plane torsional moments (M_z) that produce the elevated stresses. The two flat diaphragm options are superior in this regard, since the bonds are loaded more uniformly, resulting in lower stress levels.

4.3 System-level performance

In order to determine the optical consequences associated with these three diaphragm designs, the system-level model described in Section 3.1 was modified to include each of the diaphragm designs. After re-optimizing the diaphragm position and adjusting the large whiffletree triangle counterweights as described in Section 3.4 the predicted thermal distortion and lateral gravity print-through of the three designs were compared on a consistent basis.

4.3.1 Thermal distortion

The predicted thermal distortion surface errors are shown in Figure 12. The stress relieving features in Option-2 were shown to work remarkably well, reducing the thermal distortion RMS from 3.19nm/°C (Option-1) to 1.57nm/°C. The slotted rim added to Option-3 reduces the thermal distortion to 2.28nm/°C, which is also a significant improvement.

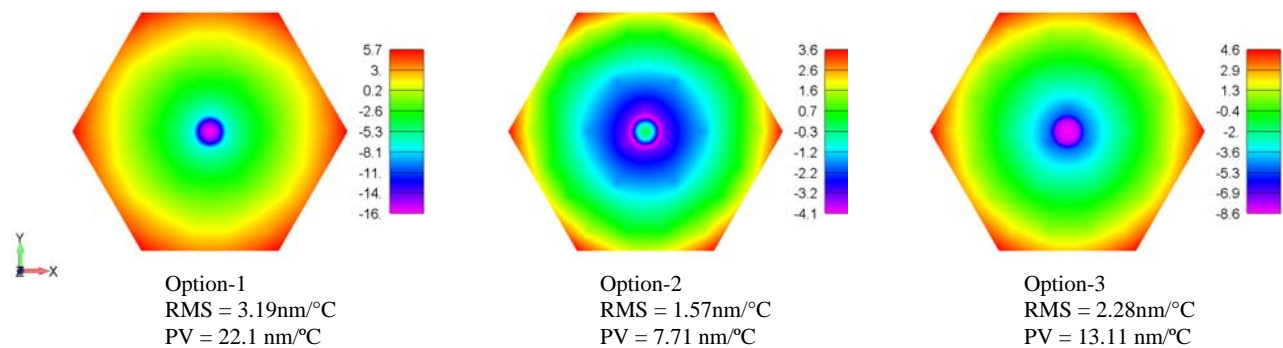


Figure 12 Thermal distortion predictions for the three diaphragm design options, (surface error, nm/°C). Option-1, flat with continuous rim (left) and Option-2, slots and convolution (center), and Option-3, flat with slotted rim (right). (Piston/Tip/Tilt subtracted)

The shape of the mirror thermal distortion is a result of two effects; 1) a global focus mode, and 2) a pronounced central bump caused by the diaphragm attachment. The global focus mode results from the CTE mismatch of the whiffletrees and the central diaphragm relative to the low expansion glass. The surface profile plot, Figure 13, shows the thermal distortion for the three designs, plotted along a trajectory between vertices at $Y=0$. Both flat diaphragms (Options 1 and 3) show a localized central depression (for a temperature increase) superimposed on the global focus mode. For Option-2, with convolution and slots, the global focus mode is reduced, and the center feature has the opposite sign, a bump rather than a depression.

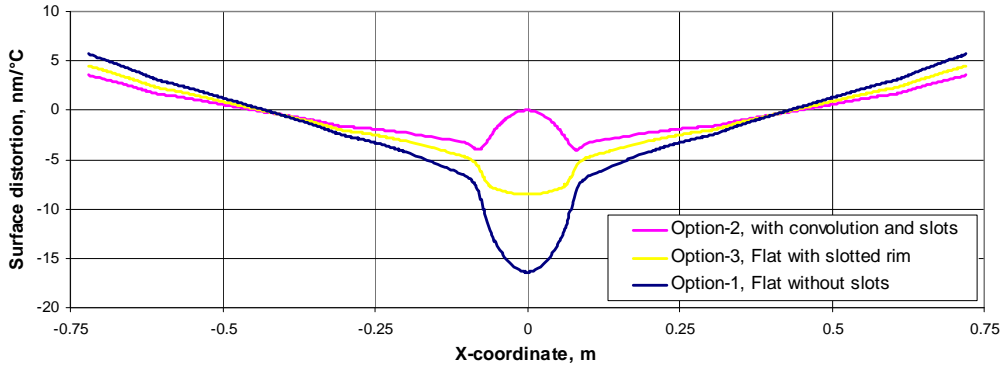


Figure 13 Surface profile plot of thermal distortion showing center bump superimposed on global focus mode for three design options. Profile trajectory is across segment vertices at $Y = 0$.

4.3.2 Lateral gravity

For TMT, the response to lateral gravity was evaluated assuming any orientation of the gravity vector relative to the segment is possible, since the segmentation pattern allows each segment to be installed in its proper location within any one of the six sectors which are 60 degrees apart around the primary array. Therefore, two orthogonal load cases are evaluated, aligned with the segment coordinate system: $1g_x$ and $1g_y$. Although the two cases are not identical, because of asymmetry inherent with the hexagonal shape, the surface deformations are found to be extremely similar in character, RMS and P-V, so only one set of results are presented here ($1g_x$).

The predicted lateral gravity surface errors for the three diaphragm designs are shown in Figure 14. Both of the flat diaphragms (Options 1 and 3) show similar results; approximately 12 nm surface error. Somewhat surprisingly, the results for Option-2 are substantially worse. It is concluded that the different load transfer mechanism for Option-2, described in Section 4.2.2, causes the larger amplitude distortion. It is also noted that the shape of the center bump is different for Option-2, having a lower spatial frequency and larger peak-to-valley amplitude.

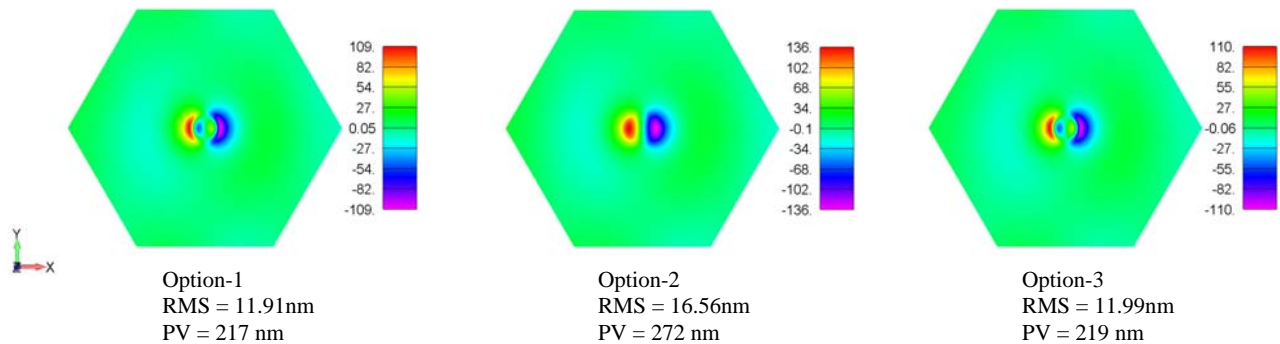


Figure 14 Predicted lateral gravity surface error (x-dir) for each diaphragm type, (nm). Option-1, flat with continuous rim (left) and Option-2, slots and convolution (center), and Option-3, flat with slotted rim (right). (Piston/Tip/Tilt subtracted)

The surface deformation profile plot, Figure 15, compares the character of the surface deformations from the three diaphragm designs. The amplitude and spatial frequency of the deformation differs for Option-2 (convolution and slots) compared to the two flat diaphragms (Options-1 and -3). The flat diaphragms introduce two local bending moments into the mirror as load is transferred at the 12- and 6-o'clock locations (as discussed in Section 4.2.2). These two moments are separated along the line of action, thus giving rise to the pair of asymmetric bumps. Conversely, Option-2 (convolution and slots) transfers loads into the mirror at the 3- and 9-o'clock locations (as described in Section 4.2.2), resulting in a single combined moment with twice the magnitude, centered along the line of action.

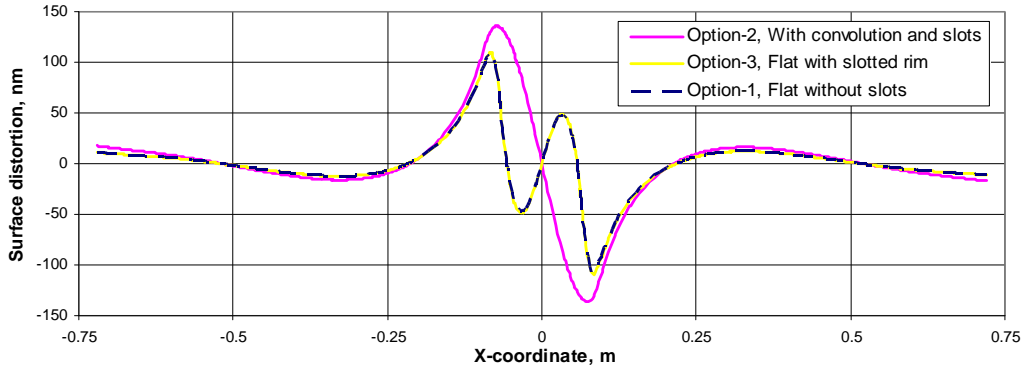


Figure 15 Surface profile plot of lateral gravity distortion for the three diaphragm design options. Profile trajectory is across segment vertices at $Y = 0$, for the $1g_x$ load case.

4.4 Preferred diaphragm design

Optical performance results are summarized in Table 2 for the three diaphragm designs. Each design has similar *Axial gravity* performance, which is expected since all three configurations utilize the same axial support systems. Thus, axial gravity performance is not a differentiating factor in evaluating the design options.

Comparing the *Thermal distortion* and *Lateral gravity* results, Option-2 is extremely good for thermal distortion, but with significantly higher surface figure error when subject to lateral gravity. Since lateral gravity distortion is of high spatial frequency, the optical consequences in the telescope are more significant than the thermal distortion errors which contain a significant amount of low-order error, as discussed in Section 3. Based on this, the lowest lateral gravity distortion is selected and a slightly larger thermal distortion effect is accepted. Option-3 (flat diaphragm with a slotted outer rim) is found to be the best compromise. This design has good lateral gravity performance, and improved thermal performance, compared to the un-slotted flat diaphragm, Option-1, therefore the flat diaphragm with the slotted outer rim (Option-3) was chosen as the baseline for the TMT Segment Support Assembly.

Diaphragm Type	Thermal distortion surface error (nm/°C)		Axial gravity surface error ($1g_z$) (nm)		Lateral gravity surface error (nm)			
	RMS	PV	RMS	PV	$(1g_x)$		$(1g_y)$	
					RMS	PV	RMS	PV
Option-1, Flat with un-slotted rim	3.19	22.1	10.37	60.4	11.91	217.	11.77	218.
Option-2, Convolution & slotted rim	1.57	7.71	10.69	59.7	16.56	272.	16.66	273.
Option-3, Flat with slotted rim	2.28	13.11	10.37	60.3	11.99	219.	11.83	219.

Table 2 Summary of predicted surface errors for three candidate TMT central diaphragm designs.

Another design option that we hope to study in the future is a blend of the characteristics of Option-2 and Option-3; essentially a variant of Option-2 with a less compliant convolution. Such a design might distribute the load more uniformly around the perimeter, resulting in a smoother profile, and might have a thermal distortion that is somewhere between the Option-2 result and the Option-3 result.

5. SUMMARY

A novel approach to optimizing the lateral support system has been presented that substantially reduces the surface figure error for the TMT thin meniscus mirror that is subject to lateral gravity and thermal environments. Three lateral support central diaphragm designs have also been presented and analyzed. One design, having stress relieving features, performs extremely well with regard to thermal distortion, but is optically inadequate when resisting lateral gravity. Finally, the preferred central diaphragm was selected for TMT; a flat diaphragm with a slotted outer rim, providing a good compromise between thermal distortion and lateral gravity performance.

ACKNOWLEDGEMENTS

The authors gratefully acknowledge the support of the TMT partner institutions. They are the Association of Canadian Universities for Research in Astronomy (ACURA), the California Institute of Technology and the University of California. This work was supported as well by the Gordon and Betty Moore Foundation, the Canada Foundation for Innovation, the Ontario Ministry of Research and Innovation, the National Research Council of Canada, the Natural Sciences and Engineering Research Council of Canada, the British Columbia Knowledge Development Fund, the Association of Universities for Research in Astronomy (AURA) and the U.S. National Science Foundation.

REFERENCES

-
- [1] Thirty Meter Telescope (TMT), <http://www.tmt.org>
 - [2] E. Ponslet; D. Blanco; M. Cho; T. Mast; J. Nelson; R. Ponchione; M. Sirota; V. Stephens; L. Stepp; A. Tubb; E. C. Williams, "Development of the Primary Mirror Segment Support Assemblies for the Thirty Meter Telescope", E. Atad-Ettinger; J. Antebi; D. Lemke, Editors, SPIE Proceedings, Vol. 6273, 2006
 - [3] C. Baffes; T. Mast; J. Nelson; E. Ponslet; V. Stephens; L. Stepp; E. C. Williams, "Primary Mirror Segmentation Studies for the Thirty Meter Telescope" SPIE Proceedings, Marseille, 2008.
 - [4] W. M. Keck Observatory and telescopes, <http://www.keckobservatory.org>
 - [5] T. Mast and J. Nelson, "The Status of the W. M. Keck Observatory and Ten Meter Telescope," in *Large Optics Technology*, SPIE Proceedings, Vol. 571, 1985
 - [6] Southern African Large Telescope (SALT), <http://www.salt.ac.za>
 - [7] J. Swiegers and H. Gajjar, "Completion of the Southern African Large Telescope (SALT) Primary Mirror System," in *Ground-based Telescopes*, J. M. Oschmann, Editor, SPIE Proceedings, Vol. 5489, pp. 881-891, 2004
 - [8] D. A. H. Buckley; J. G. Meiring; J. Swiegers; and G. Swart, "Many segments and a few dollars: SALT solutions for ELTs," in *Second Bäckaskog Workshop on Extremely Large Telescopes*, A. L. Ardeberg & T. Andersen, Editors, SPIE Proceedings, Vol. 5382, pp. 245-256, 2004
 - [9] D. Blanco *et al.*, "The SALT Mirror Mount: a high performance, low cost mount for segmented mirrors," in *Future Giant Telescopes*, J. R. Angel & R. Gilmozzi, Editors, SPIE Proceedings, Vol. 4840, pp. 527-532, 2003
 - [10] FEMAPTM Users Manual, Version 9.3, UGS Corporation, www.ugs.com
 - [11] NX NASTRANTM V5 Users Manual, UGS Corporation, www.ugs.com
 - [12] SigFit Reference Manual, Version 2004-R1. Sigmadyne Inc, <http://www.sigmadyne.com>